Frontiers in Heat and Mass Transfer

Tech Science Press

https://doi.org/10.32604/fhmt.2026.084530

ARTICLE

Effect of Surface Roughness on Flow Behavior and Conjugate Heat Transfer between TBC and Cooling Film

Yuzhang Wang[1,2,*], Zhuning Liu[1], Haozhe Sun[1], Zhuo Li[3], Kanru Cheng[1] and Chaoran Yang[1]

[1]School of Mechanical Engineering, Shanghai Jiao Tong University, 800 Dong Chuan Rd., Shanghai, China
[2]Key Laboratory for Power Machinery and Engineering of Ministry of Education, Shanghai Jiao Tong University, 800 Dong Chuan Rd., Shanghai, China
[3]State Key Laboratory of Pollution Control and Resource Reuse, College of Environmental Science and Engineering, Tongji University, 1239 Siping Road, Shanghai, China

*Corresponding Author: Yuzhang Wang. Email: yuzhangwang@sjtu.edu.cn

Received: 24 April 2026; Accepted: 30 June 2026; Published: 31 August 2026

ABSTRACT: During the operation of a gas turbine, the surface morphology of thermal barrier coatings (TBCs) of the high temperature blades inevitably evolves due to sintering, particle deposition or other factors, leading to an increase in surface roughness. This altered roughness can significantly influence the flow behavior of cooling films and the heat transfer performance of the coupled cooling film-TBC system. In this work, the flow behavior and conjugate heat transfer between cooling film and TBC under varying surface roughness conditions were investigated using the double distribution function lattice Boltzmann method (DDF-LBM) coupled with large eddy simulation (LES). The effects of surface roughness on the vortex structures, mean velocity profile, surface shear stress distribution, mean shear stress, surface temperature distribution, field synergy distribution, and mean heat transfer coefficient were analyzed. The results demonstrate that increased TBC surface roughness substantially enhances flow mixing, as evidenced by more widespread vortex distributions (identified by Ω criterion), modifications to the mean velocity profile, and increases in both the displacement and momentum thicknesses of the boundary layer. Moreover, surfaces with greater roughness exhibit more pronounced non-uniformities in shear stress and temperature distributions, which may induce cracking due to uneven mechanical loads and thermal stresses, thereby accelerating TBC degradation. The mean dimensionless surface temperature of the TBC increases by approximately 130%. Additionally, surface roughness augments heat transfer performance, with the convective heat transfer coefficient rising by up to 19.12%, and this phenomenon can be explained by the gradually saturated Field synergy distribution.

KEYWORDS: Thermal barrier coating; film cooling; surface roughness; double distribution function lattice Boltzmann method; large eddy simulation

1 Introduction

With the increasing demand for gas turbines and aeroengines with higher efficiency and better power performance, harsher operating conditions caused by continuously rising of turbine inlet temperature (TIT) lead to higher requirements for the cooling design of turbine blades [1,2]. In order to protect turbine blades from excessively high TIT, external cooling technologies, namely thermal barrier coating (TBC) and film cooling, are applied and contribute the majority of the increase of the temperature capability in recent decades [3,4]. Thermal barrier coating is a multi-layer porous structure, generally composed of top coat (TC), bond coat (BC), and thermally grown oxide (TGO) [5]. Featured with low effective thermal conductivity that can be credited to the material properties and porous internal structures, TBC has an extensive industrial application for the thermal protection in aerospace, marine, and power generation [6]. TBC makes considerable contributions to the rise of temperature capacity of turbine blade, without increasing the consumption of the coolant extracted from compressor, which may negatively affect the overall efficiency of turbine. Film cooling is another external cooling technology, which utilizes the outflow of the internal cooling to form a gas film between the high temperature mainstream flow and the turbine blade [7]. The effectiveness of film cooling can be affected by a handful of factors, including but not limited to turbulent intensity [8], blowing ratio, film hole configuration [9], and surface microstructures [10]. In many studies on the heat transfer properties and flow behaviors of cooling film, the TBC surface is assumed to be an idealized smooth plane without surface roughness microstructures. But a lot of other research on the microscopic surface morphology of TBC does not support this hypothesis [6]. Therefore, the study on the influence of TBC surface roughness on the inter-coupling heat transfer between TBC and cooling film is helpful to master the law of comprehensive cold effect degradation of high temperature blades during service. This is of great significance for the development of advanced gas turbines.

The surface microstructures of the TBC originate from the preparation process, and evolve along with the deterioration of TBC after gas turbine is in service [11,12]. Although many preparation techniques (plasma spraying (PS), electron beam physical deposition (EB-PVD), high velocity oxy fuel (HVOF)) [13] and new materials (pyrochlores, perovskite, monazite, lanthanum magnesium hexa-aluminate, LTA) [6] have been developed for the manufacture of TBC, the yttria stabilized zirconia (YSZ) is still the currently most well-established TBC material and the atmospheric plasma spraying (APS) is considered to be the most widely used preparation method contemporarily [14]. The as-deposited APS-TBC composed of overlapping splats, exhibits lamellar structure [15] and forms surface microstructures [13] inevitably after preparation. And after the turbine is in service, along with the deterioration of TBC, its surface microstructures change correspondingly. In harsh operating environment, a variety of factors may contribute to the deterioration of TBC, such as the corrosion of CMAS, displacement caused by TGO growth, microstructure changes induced by sintering, phase transformation, and cracks [5,12,14]. These will cause a large increase in the surface roughness of TBC.

Although many studies evaluate the external cooling performance by adiabatic effectiveness, or consider the TBC surface as an idealized surface with uniformly-distributed temperature, the heat transfer in the TBC and in cooling film are strongly inter-coupled with each other, and the best film cooling configuration for case with and without TBC can differ from each other considerably [16,17]. The surface roughness microstructures can exert a non-negligible influence on the hydrodynamic behaviors and heat transfer properties of the flow [18]. Numerous studies have been conducted on the turbulent flow over the roughness surface [18–24], investigating the influence of surface roughness on the momentum and energy transport performances. But current understanding of this problem is still limited, and the lack of consensus on this subject can be attributed to the sophisticated and random features of turbulent flow and surface roughness [25].

The real TBC is a porous layer, with complicated surface and internal microstructures resulting from the preparation process and the deterioration after gas turbine is in service. In order to study the inter-coupling heat transfer and flow behavior of cooling film and TBC, an approach for the numerical reconstruction of TBC is needed to acquire the geometry of TBC with given parameters and features, such as porosity, mean square root roughness, and shape constraint of internal defects. For the reconstruction of rough surface, plenty of methods have been developed to model the rough surface with Gaussian or non-Gaussian ordinate distribution [26]. The Fast Fourier Transform (FFT) method is a well-studied approach for generating surface roughness microstructures. Many FFT-based methods for rough surface modeling and their modifications are available. The numerical reconstruction of porous media is also studied extensively. The quartet structure generation set (QSGS) method developed by Wang et al. [27], is a widely adopted method for generation of porous media in microscopic pore scale studies. The Pore Crack Particle microstructure reconstruction (PCPMR) method, developed by Long et al. [28], proposed a reconstruction of TBC with internal defects verified by comparison of reconstructed geometry with SEM images and comparison of simulation results with experimental data on the heat transfer properties of the reconstructed model, which is used in this work.

The numerical research of inter-coupling heat transfer between cooling film and TBC involves complex geometry (porous TBC), and Lattice Boltzmann Method (LBM) is a well-suited approach for such simulation [29]. LBM was developed by McNamara and Zanetti [30] from the Lattice Gas Automation, and then found to be theoretically independent from LGA by He and Luo [31], who proved that the LBM is a special discretized form of the Boltzmann Equation. Nowadays, LBM has become a well-established and extensively-used scheme for various problems. To extend the LBM to thermo-hydrodynamics, many single population models and two population models have been developed. Among these models, the Double Distribution Function Lattice Boltzmann Method (DDF-LBM) proposed by He et al. [32] is a widely used approach for Advection-Diffusion problems, featuring better numerical stability compared with multispeed schemes. Additionally, by incorporating turbulent models like Reynolds averaging Navier-Stokes (RANS), Large Eddy Simulation (LES) or Direct Numerical Simulation (DNS), the LBM is also capable of simulating heat and mass transfer in turbulent flow [33–35]. Compared with RANS and DNS, LES offers balanced accuracy and moderate cost in computation and storage, by resolving large-scale turbulence which plays an important role in heat and mass transfer and using sub-grid model to model the small-scale turbulence with inferior importance. These merits allow a wide range of applications in many studies for LES, especially in simulations of the film cooling [36,37].

In this work, the microscale flow behavior and conjugate heat transfer model based on DDF-LBM with LES was developed, which was used to study the effect of the evolution of the surface morphology of the thermal barrier coating in service on the comprehensive cooling effect of the high temperature blade surface. Using the numerical reconstruction method of PCPMR developed by our team, the geometric microstructure of TBC can be characterized for different service times with high accuracy. The performance of conjugate heat transfer and flow behavior was investigated under different TBC surface roughness, and some flow characteristics (Ω criterion, velocity profile and velocity difference profile, shear stress, etc.) and conjugate heat transfer performance (temperature distribution, synergy between temperature field and velocity field, heat transfer properties, mean heat transfer coefficient, etc.) were analyzed in detail. Also, the relation of mean shear stress on the TBC surface to surface roughness and velocity profile was analyzed.

2 Methodology

2.1 Reconstruction of Thermal Barrier Coating

As previously mentioned, the top coat of TBC is a layer of porous media, with complex internal defects and surface roughness microstructures after gas turbine is in service. The rough surfaces generated by FFT can accurately reproduce the statistical characteristics of actual TBC surfaces, and the overall similarity of the geometric profiles is high. To reconstruct the geometry of the TBC correctly, the FFT method and the PCPMR method are adopted for the reconstruction of the internal and surface microstructures respectively.

2.1.1 Reconstruction of Thermal Barrier Coating Surface Roughness Microstructures

The exact morphology of a given rough surface usually exhibits a strong randomness, and thus, the statistical properties of the surface roughness are widely used in the studies of the reconstruction and description of the rough surface. The statistic properties of the surface roughness are usually described by the first to fourth central moments, which represent the arithmetic mean roughness (S_a), the mean square root roughness (S_q), the skewness (S_{sk}) and the kurtosis (S_{ku}) of the rough surface respectively.

$$\begin{cases} S_a = \dfrac{1}{A}\iint_A |z-\overline{z}|\,dS \\ S_q = \sqrt{\dfrac{1}{A}\iint_A (z-\overline{z})^2\,dS} \\ S_{sk} = \sqrt[3]{\dfrac{1}{A}\iint_A (z-\overline{z})^3\,dS} \\ S_{ku} = \sqrt[4]{\dfrac{1}{A}\iint_A (z-\overline{z})^4\,dS} \end{cases} \tag{1}$$

In this work, the Fast Fourier Transform method is used for the reconstruction of the surface roughness microstructures. A 2-dimension random array $\eta(i,j)$, is generated and processed with Fourier transform.

$$S_\eta\left(\omega_x,\omega_y\right) = \int_{-\infty}^{+\infty}\int_{-\infty}^{+\infty} \eta(x,y)\,e^{-i2\pi\left(\omega_x x+\omega_y y\right)}dxdy \tag{2}$$

The autocorrelation length l is defined as the critical length when the autocorrelation function equals zero. And an array of the autocorrelation function, $S(k,l)$, is generated based on the autocorrelation length l. And the power spectral density of the output of the filter is acquired by applying Fourier transform to the autocorrelation function array.

$$S\left(\omega_x,\omega_y\right) = \int_{-\infty}^{+\infty}\int_{-\infty}^{+\infty} S(x,y)\,e^{-i2\pi\left(\omega_x x+\omega_y y\right)}dxdy \tag{3}$$

The power spectral density function depends on the distribution of the roughness height. For example, the power spectral density function of the gaussian roughness distribution is given as below.

$$S\left(\omega_x,\omega_y\right) = \left(S_q\right)^2\frac{l_x l_y}{4\pi}e^{-\left(\omega_x^2 l_x^2+\omega_y^2 l_y^2\right)} \tag{4}$$

The l_x, l_y in the equation above is the autocorrelation length of x and y direction.

The corresponding transfer function of the power spectral density can be derived. And the filter coefficient can be acquired through an inverse Fourier transform.

$$H\left(\omega_x,\omega_y\right) = \sqrt{\frac{S_\eta\left(\omega_x,\omega_y\right)}{S\left(\omega_x,\omega_y\right)}} \tag{5}$$

$$h(x,y) = \int_{-\infty}^{+\infty}\int_{-\infty}^{+\infty} H\left(\omega_x,\omega_y\right)e^{i2\pi\left(\omega_x x+\omega_y y\right)}dxdy \tag{6}$$

And the roughness height distribution ($z(i,j)$) can be calculated by the convolution of the 2-dimension random array and the filter coefficient.

$$z(i,j) = \sum_{k=1-\frac{n}{2}}^{-1+\frac{n}{2}}\sum_{l=1-\frac{m}{2}}^{-1+\frac{m}{2}} h(k,l)\,\eta(i+k,j+l) \tag{7}$$

2.1.2 Reconstruction of Internal Microstructures

The Pore Crack Particle Microstructure Reconstruction method is capable for correct reconstruction of the porous TBC with internal defects, such as cracks, particle erosion, CMAS corrosion, and TGO growth. Based on the Quartet Structure Generation Set method, the PCPMR method introduces a series of shape constraint factors additionally for the reconstruction of internal defects of TBC. The PCPMR method is verified by comparing the reconstruction result with real scanning electron microscope images of TBC, and the effective thermal conductivity of the reconstructed TBC calculated by LBM is in good accordance with experimental results in published literature. Detailed information of PCPMR method can be found in the literature [17,28].

2.2 Computational Scheme

2.2.1 Lattice Boltzmann Method

The governing equation of LBM can be directly derived from Boltzmann Equation by the discretization in time, space and velocity. In order to simplify the double integral collision operator, the BGK model [38], which is a linear approximation near the equilibrium distribution, is adopted. The τ in the equation is the relaxation time of the collision term.

$$f_\alpha\left(\vec{r}+\vec{v}\Delta t, t+\Delta t\right)-f_\alpha\left(\vec{r}, t\right)=-\frac{\Delta t}{\tau}\left(f_\alpha\left(\vec{r}, t\right)-f_\alpha^{eq}\left(\vec{r}, t\right)\right) \tag{8}$$

Taking the accuracy of simulation result into consideration, a D3Q19 model is adopted, and the discrete velocity vectors can be determined by Eq. (9) [4,17,39]. The corresponding weight is given as Eq. (10).

$$\vec{e}_i=\begin{cases}(0,0,0), i=0\\(\pm1,0,0),(0,\pm1,0),(0,0,\pm1), i=1\sim6\\(\pm1,\pm1,0),(0,\pm1,\pm1),(\pm1,0,\pm1), i=7\sim18\end{cases} \tag{9}$$

$$w_i=\begin{cases}\frac{1}{3}, i=0\\\frac{1}{18}, i=1\sim6\\\frac{1}{36}, i=7\sim18\end{cases} \tag{10}$$

2.2.2 Double Distribution Function Lattice Boltzmann Method

The Double Distribution Function Lattice Boltzmann Method is a widely used thermal LBM approach. In the DDF-LBM, two sets of distribution function, namely the particle distribution function and the temperature distribution function, are calculated separately in order to simulate the evolution of the flow field and temperature field. According to the Chapman-Enskog analysis, the relaxation times of these two equations can be calculated from the kinematic viscosity and the thermal diffusivity respectively.

$$\begin{cases}f_i\left(\vec{r}+\vec{v}\Delta t, t+\Delta t\right)-f_i\left(\vec{r}, t\right)=-\frac{\Delta t}{\tau_f}\left(f_i\left(\vec{r}, t\right)-f_i^{eq}\left(\vec{r}, t\right)\right)\\g_i\left(\vec{r}+\vec{v}\Delta t, t+\Delta t\right)-g_i\left(\vec{r}, t\right)=-\frac{\Delta t}{\tau_g}\left(g_i\left(\vec{r}, t\right)-g_i^{eq}\left(\vec{r}, t\right)\right)\end{cases} \tag{11}$$

$$\tau_f=\frac{\nu}{{c_s}^2\Delta t}+\frac{1}{2}, \tau_g=\frac{\alpha}{{c_s}^2\Delta t}+\frac{1}{2} \tag{12}$$

The equilibrium distribution function can be calculated from the local density, temperature and macroscopic velocity.

$$\begin{cases} f_i^{eq} = w_i \rho \left(1 + \dfrac{\vec{e}_i \cdot \vec{u}}{c_s{}^2} + \dfrac{(\vec{e}_i \cdot \vec{u})^2}{2c_s{}^4} + \dfrac{\vec{u}^2}{2c_s{}^2}\right) \\ g_i^{eq} = w_i T \left(1 + \dfrac{\vec{e}_i \cdot \vec{u}}{c_s{}^2}\right) \end{cases} \tag{13}$$

The macroscopic parameters like the density, temperature, and velocity are the moments of the particle and temperature distribution function.

$$\begin{cases} \rho = \sum\limits_i f_i \\ T = \sum\limits_i g_i \\ \vec{u} = \sum\limits_i \left(\dfrac{f_i}{\rho} \vec{e}_i\right) \end{cases} \tag{14}$$

For the temperature distribution function, a separate subgrid thermal diffusivity correction is introduced: based on turbulence Prandtl number assumptions, the subgrid thermal diffusivity is correlated with subgrid eddy viscosity to correct subgrid transport in the temperature field. The slight dynamic relaxation time is adjusted based on the flow field gradient to suppress numerical oscillations caused by thermal coupling and ensure global computational stability.

2.2.3 Lattice Boltzmann Method with Large Eddy Simulation

In order to correctly simulate the highly turbulent flow of the cooling film over the rough surface of TBC, the Large Eddy Simulation is adopted. To implement the LES in the scheme of LBM, the Deardoff function is used to filter the particle distribution function of LBM.

$$G(x, x') = \begin{cases} \dfrac{1}{\Delta x_1 \Delta x_2 \Delta x_3}, \left|x_i - x_i^{'}\right| \le \dfrac{\Delta x_i}{2}, i = 1, 2, 3 \\ 0, \left|x_i - x_i^{'}\right| \le \dfrac{\Delta x_i}{2}, i = 1, 2, 3 \end{cases} \tag{15}$$

$$\overline{f_i} = \int f_i(x) \, G(x, x') \, dx' \tag{16}$$

The filtered lattice BGK-Boltzmann equation can be derived as below.

$$\overline{f_i}(\vec{r} + \vec{v}\Delta t, t + \Delta t) - \overline{f_i}(\vec{r}, t) = -\frac{\Delta t}{\tau_f}\left(\overline{f_i}(\vec{r}, t) - \overline{f_i^{eq}}(\vec{r}, t)\right) \tag{17}$$

In LBM-LES, the relaxation time is calculated form the total viscosity, which is the sum of the eddy viscosity and the molecular viscosity.

$$\tau_f = \frac{\nu_t}{c_s{}^2 \Delta t} + \frac{1}{2} \tag{18}$$

$$\nu_t = \nu_e + \nu \tag{19}$$

The eddy viscosity (ν_e) can be acquired by the Smagorinsky model.

$$\nu_e = C\Delta^2 \left|\overline{S}\right| \tag{20}$$

In the equation above, C is the Smagorinsky constant, $\Delta = (dx \cdot dy \cdot dz)^{\frac{1}{3}}$ is the filter width. The S is the local strain tensor, which can be calculated from non-equilibrium moment tensor under the LBM scheme.

$$S_{ij} = \frac{1}{2}\left(\frac{\partial u_i}{\partial x_j} + \frac{\partial u_j}{\partial x_i}\right) = -\frac{1}{2\rho {c_s}^2 \tau_t}\left(\sum_k \left(\overrightarrow{e_{ki}} \cdot \overrightarrow{e_{kj}}\left(f_i - f_i^{eq}\right)\right)\right) \tag{21}$$

Additionally, in order to correct the overestimation of sub-grid stress near the wall [40], the Van Driest damping function is applied, with the Van Driest parameter $A^+ = 26$.

$$V_{A^+} = 1 - e^{-\frac{y^+}{A^+}} \tag{22}$$

2.3 Model Validation

In order to verify the reliability of DDF-LBM and LBM-LES algorithms, the simulations of heat conduction in porous media and plate Poiseuille flow are conducted respectively. The simulation results of heat conduction in porous media show good accordance with the experimental results [4], as shown in Table 1. In this experiment, the layered coating of 146 mm was prepared by APS. Its material is 8YSZ, and its porosity is 13.7%. Netzsch DSC204 was used to measure the specific heat capacity at constant pressure. The Cape-Lehman model was used to measure the thermal diffusivity of the coating, and the pulse correction was performed. This indicates that the model developed can analyze the heat transfer performance within the thermal barrier coating with high accuracy.

Table 1: Validation of the DDF-LBM.

Temperature/°C	$\overline{\lambda_{\text{exp}}}/\left(\text{W} \cdot \text{m}^{-2} \cdot \text{K}^{-1}\right)$	$\overline{\lambda_{cal}}/\left(\text{W} \cdot \text{m}^{-2} \cdot \text{K}^{-1}\right)$	Relative Error (%)
200	1.56	1.54	1.26
400	1.52	1.50	1.32
600	1.45	1.45	0.21
800	1.43	1.44	0.70
1000	1.49	1.47	1.34

In order to verify the accuracy of the modeling used to analyze the surface flow characteristics and flow structure of the thermal barrier coating, the model was used to analyze the plate Poiseuille flow. Periodic boundary conditions are applied in the streamwise (x) and spanwise (z) directions, and no-slip boundary conditions are applied at the wall. The computational domain sizes are $L_x = 8\pi\delta$ and $L_z = 3\pi\delta$, where δ is the channel half-width. The flow is driven by a uniform pressure gradient. The calculation results are in good agreement with the DNS calculation [41], as shown in Fig. 1. It is shown that the model is effective in capturing the details of complex flows near the wall. In the transition zone ($10 < y^+ < 100$), the calculation speed is slightly lower than the DNS result, with the maximum error of 4.96%. In the log layer ($y^+ > 100$) region, the calculation results are in good agreement with the DNS simulation results, with the maximum error of only 1.8%. And the grid independence validation is also conducted on the plate Poiseuille flow, as shown in Table 2, the Fanning friction factor is in good agreement with Yao's DNS simulation result [42] ($C_{f0} = 8.16 \times 10^{-3}$). Taking the computation cost and accuracy into consideration, the lattice length $l = 5.0$ μm is chosen.

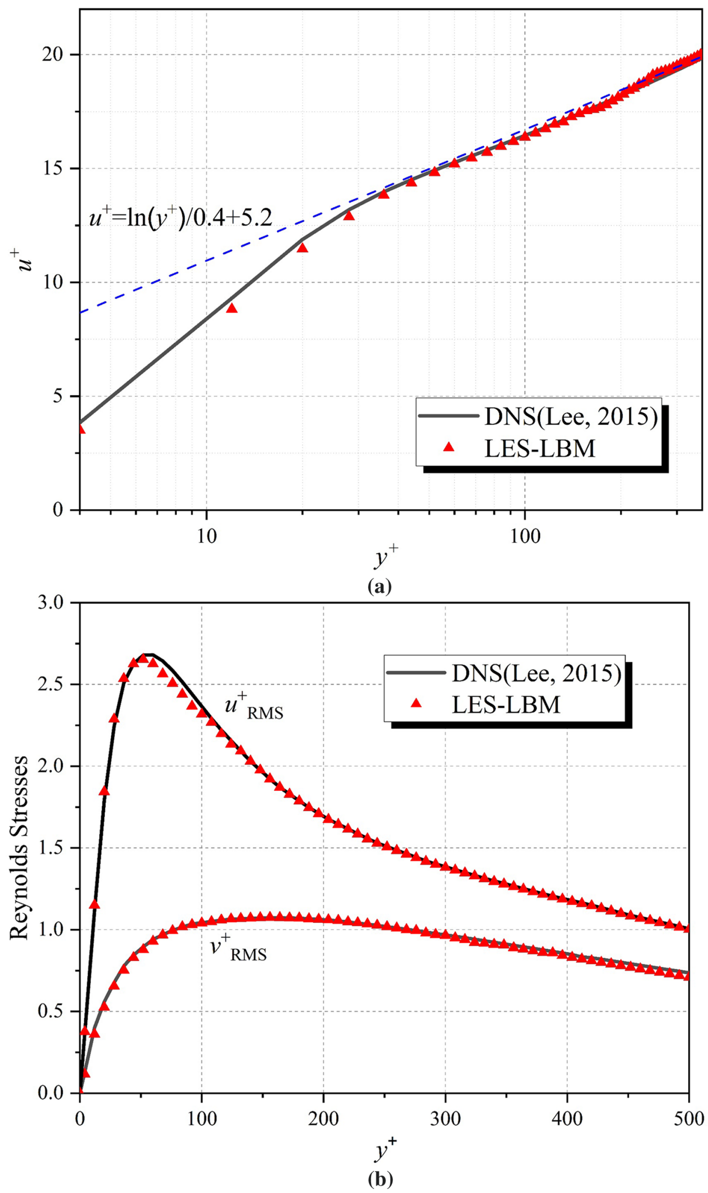

Figure 1: Validation of LES-LBM. (**a**) Flow direction average velocity distribution. (**b**) Reynolds stress distribution.

Table 2: Validation of the LBM-LES and grid independence.

Lattice Length/μm	Mesh Quantity	$C_f\ (\times 10^{-3})$	Relative Error (%)
10.0	128 × 64 × 64	8.95	9.68
7.5	171 × 86 × 86	8.33	2.08
5	256 × 128 × 128	8.08	0.98
2.5	512 × 256 × 256	8.06	1.22

2.4 Boundary Condition and Setup

The boundary conditions used in the present simulations were extracted from a high-fidelity CFD simulation of a GEE3 vane operating under representative engine conditions. In the CFD model, the mainstream temperature was 1570°C, while the coolant temperature was 610°C. The blowing ratio of the single film-cooling hole was maintained at 0.5. Fig. 2 presents the flow and thermal fields obtained from the CFD simulation around the film-cooling hole. To investigate the influence of surface roughness on the conjugate heat transfer characteristics of the TBC and the cooling film, a cuboid computational domain was extracted from the downstream region where the film-cooling flow was fully developed, as illustrated in Fig. 2. In this region, the coolant film exhibited a stable flow structure, and the velocity at the upper boundary of the cooling film remained approximately 33 m/s. Meanwhile, the temperature distributions at the top of the cooling film and within the bond-coat layer were nearly uniform and constant, with values of 1250°C and 845°C, respectively. A series of numerical simulations were conducted on the 1280 μm × 640 μm × 640 μm region, composed of a 540 μm thick cooling film and a 100 μm thick TBC as shown in Fig. 2, whose surface roughness are $S_q = 0, 2.5, 5, 7.5, 10, 12.5$ μm respectively, as shown in Fig. 3. The boundary conditions and the key parameters of the simulation and the macroscopic physical properties of the fluid and the solid, namely air and YSZ, are listed in Table 3. A non-equilibrium extrapolation scheme is used in the near-wall region to ensure second-order accuracy at the velocity and temperature boundaries.

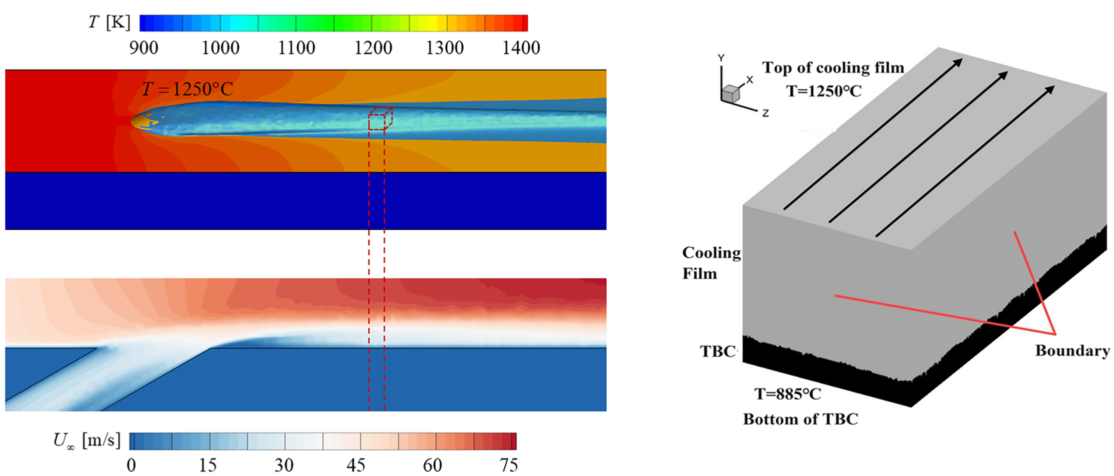

Figure 2: Geometrical model with the boundary conditions.

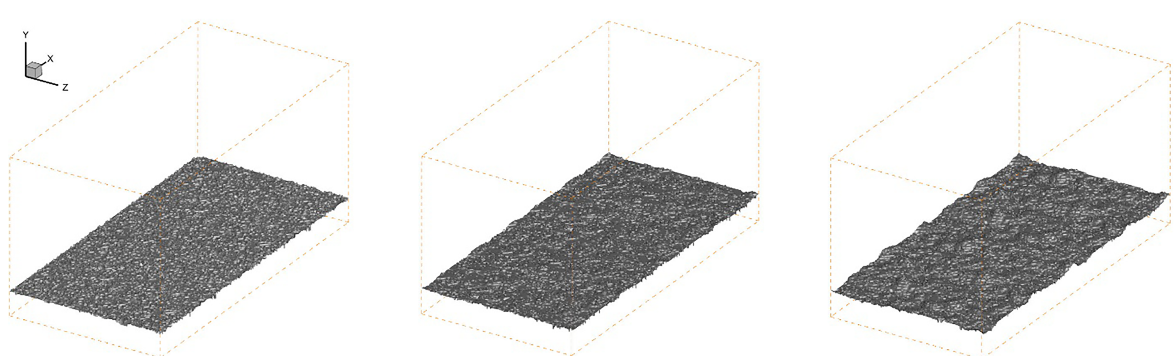

(a) Sq = 0 μm **(b)** Sq = 2.5 μm **(c)** Sq = 5.0 μm

Figure 3: (continued)

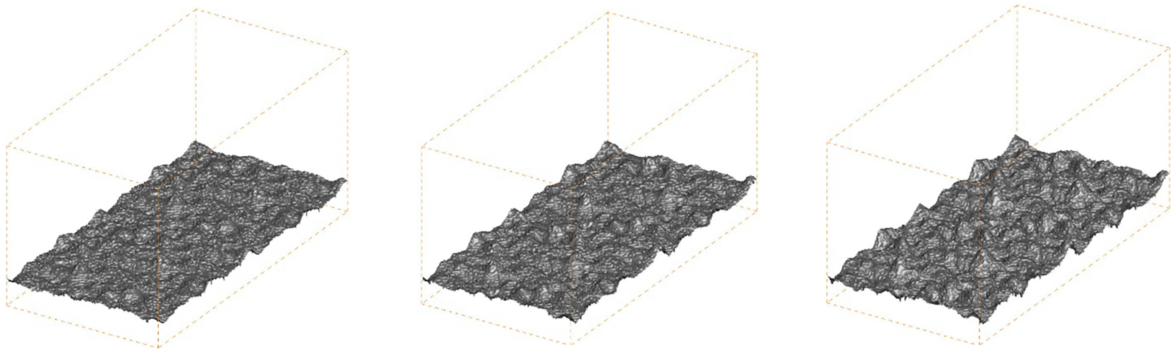

Figure 3: TBC models with different surface roughness.

Table 3: Boundary condition and simulation setup.

Parameter	Symbol	Value
Lattice sound speed	c_s	$1/\sqrt{3}$
Thermal conductivity of air $(\text{W} \cdot \text{m}^{-2} \cdot \text{K}^{-1})$	λ_1	0.0807
Thermal conductivity of YSZ $(\text{W} \cdot \text{m}^{-2} \cdot \text{K}^{-1})$	λ_2	2.43
Kinetics viscosity of air $(\text{m}^2 \cdot \text{s}^{-1})$	ν	1.6585×10^{-5}
Velocity at the top of the cooling film $(\text{m} \cdot \text{s}^{-1})$	U_∞	33
Temperature at the top of the cooling film (°C)	T_∞	1250
Temperature at the bottom of the TBC (°C)	T_w	845

3 Result and Discussion

3.1 Computational Result

Under the scheme of DDF-LBM with LES, 6 cases of cooling film and TBC with different surface roughness ($S_q = 0.0, 2.5, 5.0, 7.5, 10.0, 12.5\ \mu\text{m}$) were investigated. The velocity field and temperature field of each case were acquired. In Fig. 4, the geometries of TBC surface with different surface roughness, velocity magnitude distribution normalized by maximum, and non-dimensional temperature ($\Theta = \frac{T-T_w}{T_\infty - T_w}$) are visualized. These results are further processed and analyzed in terms of the impact of surface roughness on the flow behaviors and the heat transfer performances respectively, in the following sections (Sections 3.2 and 3.3).

3.2 Flow Behaviors of Cooling Film

The effectiveness of film cooling and the life expectancy of TBC hinge on the flow behaviors of the cooling film near the TBC surface to a considerable extent. In the following sections, the influence of surface roughness on many aspects of the flow behaviors, including the vortex structures, the velocity profile, and the distribution of the shear stress on the TBC surface, is discussed respectively.

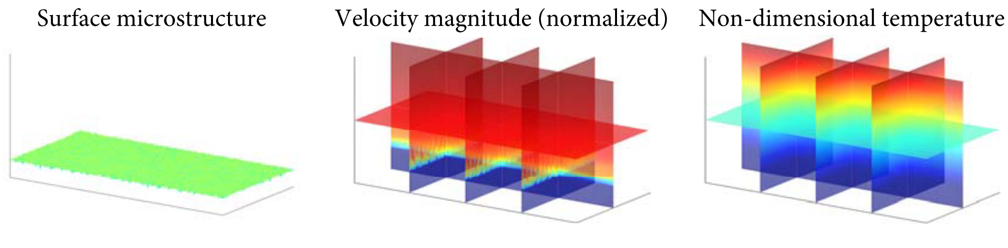

(**a**) $S_q = 0.0\mu m$

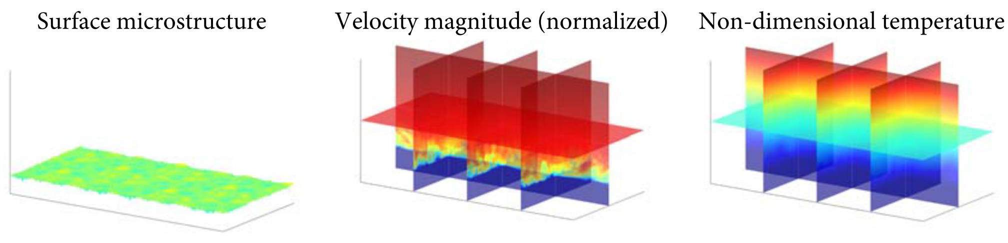

(**b**) $S_q = 2.5\mu m$

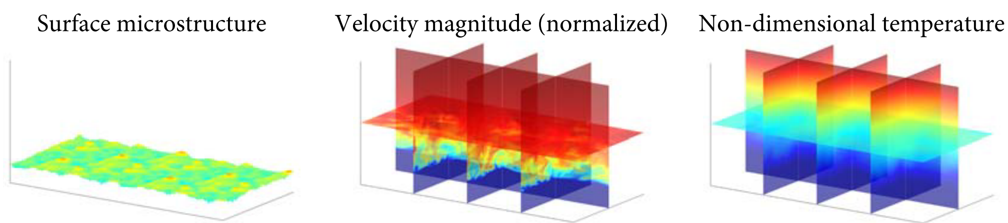

(**c**) $S_q = 5.0\mu m$

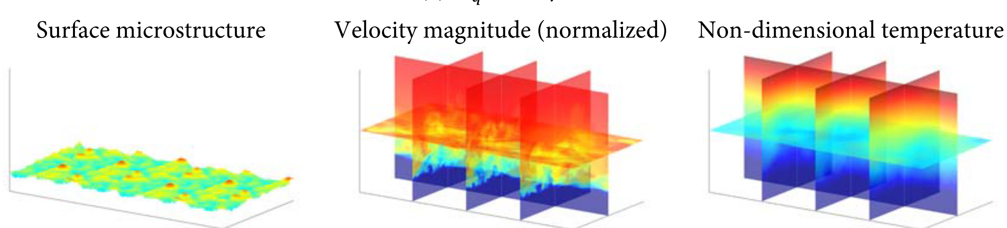

(**d**) $S_q = 7.5\mu m$

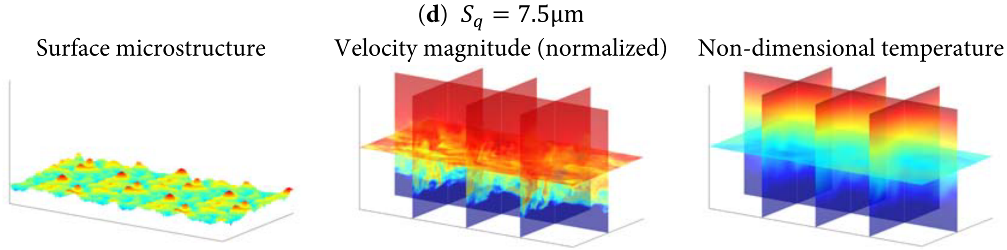

(**e**) $S_q = 10.0\mu m$

Figure 4: (Continued)

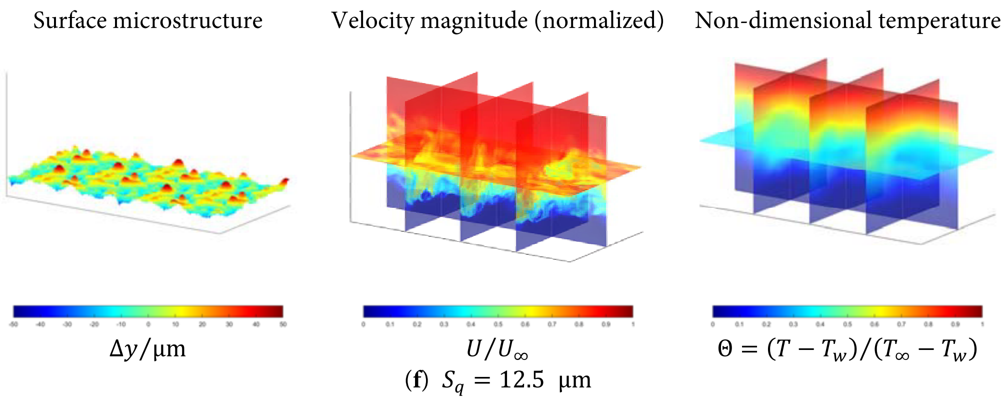

Figure 4: The morphology of the TBC surface, the velocity magnitude field (normalized), and the temperature field, for cases with different surface roughness.

3.2.1 Velocity Field

The average dimensionless velocity of the cooling film in the flow direction with different surface roughness is shown in Fig. 5. Within the flow logarithmic layer, the dimensionless average velocity of the flow direction basically satisfies the average velocity expression ($u^+ = \frac{1}{\kappa} \ln y^+ + B - \Delta u^+$) in the logarithmic region of the wall turbulent boundary layer, which is proportional to the log height. The slope difference is small, basically maintained in the range of 0.38–0.42, with some slight local fluctuations. With the increase of TBC surface roughness, the obstruction of rough elements on the flow increases, and the velocity distribution curve moves down, and the offset Δu^+ between the two adjacent curves is basically the same, and its value is about 2.

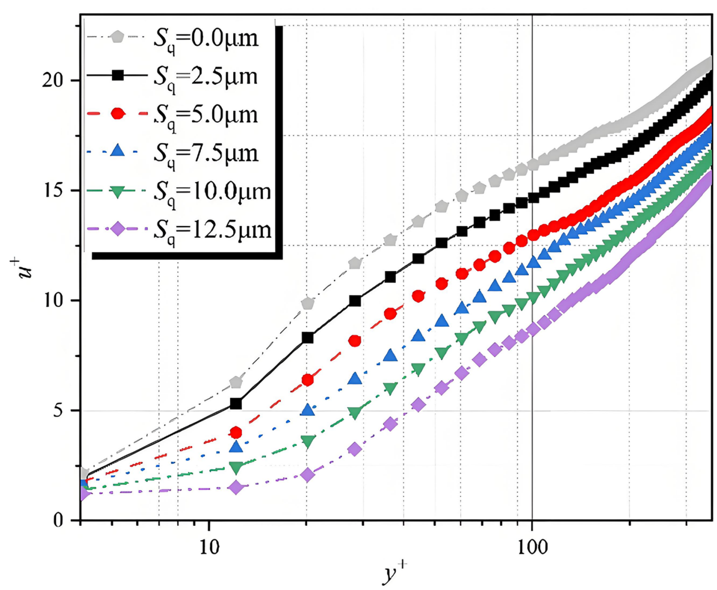

Figure 5: Distribution of flow direction average dimensionless velocity u^+.

The instantaneous velocity at $y^+ = 15$ in the x–z section is shown in Fig. 6. The instantaneous velocity shows a significant strip structure, and the introduction of sedimentary rough structure directly leads to the change of turbulent coherent structure in the near-wall region. This will lead to the increase of the shear stress of the flow. Under the strong shear stress, the high-speed strip gradually rows and slender until it starts to break or even disappear. While the low-speed strip is more twisted and winding, and the structure is no longer regular. The absolute value of the overall velocity within the section is significantly reduced, as the result of the upshift of the flow boundary layer.

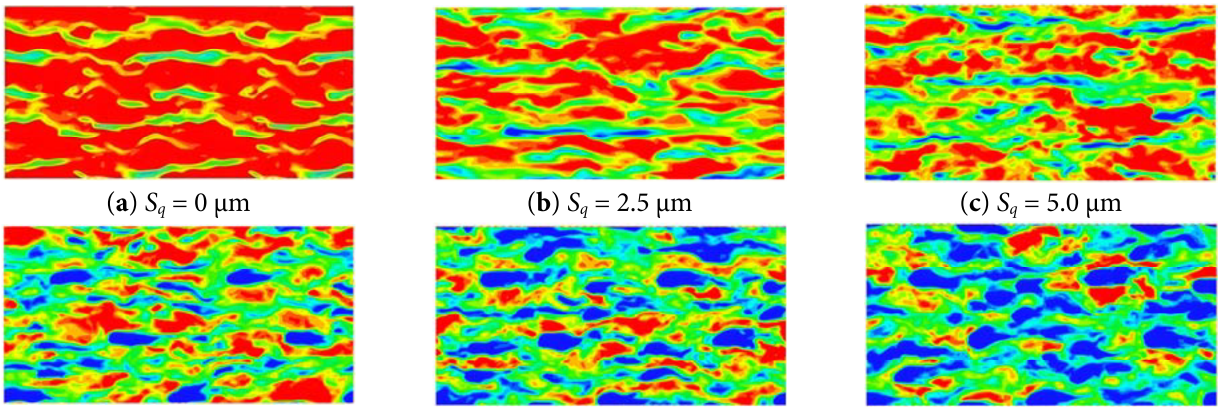
(**a**) $S_q = 0$ μm (**b**) $S_q = 2.5$ μm (**c**) $S_q = 5.0$ μm
(**d**) $S_q = 7.5$ μm (**e**) $S_q = 10.0$ μm (**f**) $S_q = 12.5$ μm

Figure 6: Instantaneous velocity distribution of x–z section at $y^+ = 15$.

3.2.2 Vortex Structures

The surface roughness microstructures cause the velocity fluctuation of fluid near the wall, and thus exert non-negligible effects on the generation and the evolution of the vortices. In order to study the influence of the surface roughness on the vortex structures, the Ω criterion, which is a widely used vortex identification method [43] developed by Liu et al. [44], is applied to the velocity field, and the iso-surface ($\Omega = 0.52$) graphs of each case colored with non-dimensional velocity magnitude are given in Fig. 7. The surface roughness microstructures greatly enhance the generation and evolution of the vortex structure. There is large scale flow vortex structure, smaller scale horseshoe vortex structure in the flow field, and small vortex system caused by the pores on the TBC surface. With the increase of roughness, the large-scale horseshoe vortex structure appears in the flow field, the vortex surface is closer to the mainstream side, and the flow rate rises. The newly formed vortices exist mainly at the top position of the rough elements, and their size and vorticity size are highly correlated with the rough elements. In the case with small surface roughness ($R_q = 2.5, 5$ μm), the vortices are mainly concentrated in the region near the TBC surface, and then along with the increase of the surface roughness ($R_q = 7.5, 10.0, 12.5$ μm), extend themselves away from the TBC surface. Besides, the marginal effect of surface roughness microstructures enhancement on the generation and evolution of the vortex structure is decreasing. The vortices induced by the surface roughness microstructures complicate the transportation of energy and momentum, and thus lead to the change of flow behaviors and heat transfer performance of the cooling film, which may pose non-negligible impact on the mechanical load (shear stress on the TBC surface), the effectiveness of the thermal protection (heat transfer coefficient), and the durability of the TBC (non-uniformity of the shear stress distribution and the temperature distribution).

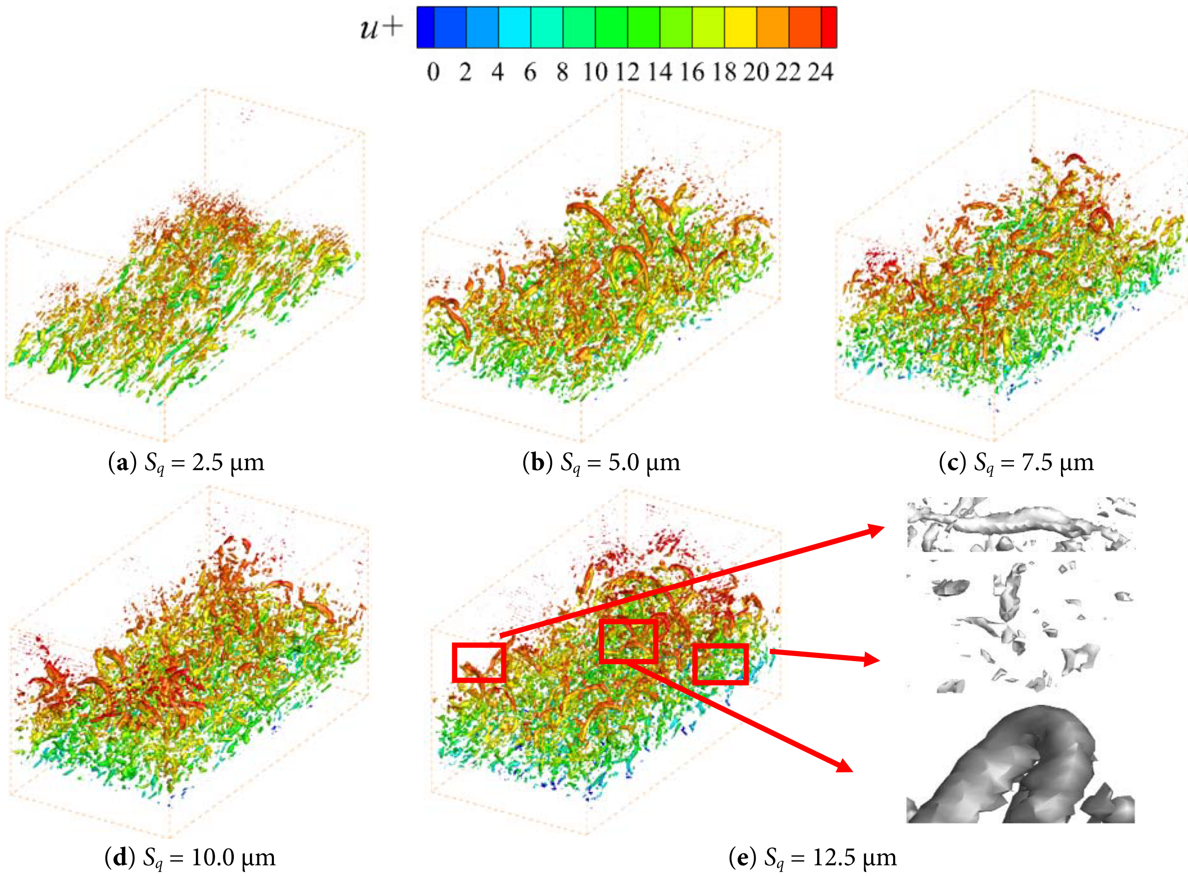

Figure 7: The iso-surface map of Ω criterion (iso-value Ω = 0.52) for cases with different surface roughness, colored with non-dimensional velocity u^+.

3.2.3 Mean Velocity Profile

The influence of the surface roughness on the vortex structures indicates that the surface roughness greatly enhances the momentum-mixing effect of the main flow, which may lead to the notable variation of the velocity profile. By averaging the velocity in horizontal direction (x direction and z direction), the mean velocity ($U^* = \frac{\overline{U}}{U_\infty}$) profile along the y direction is acquired. And the mean velocity difference ($\frac{dU^*}{dz}$) profile along the y direction can be calculated similarly as well. The results are presented respectively in Figs. 8 and 9. These 2 profiles are good references for the evaluation of the mixing effect of the flow. The mean velocity distribution near the TBC surface is changed greatly due to the influence of the sophisticated vortex structure induced by the surface roughness. The range of surface roughness' influence on the velocity profile expands with the TBC surface roughness. As the surface roughness of TBC increases, the velocity near the coating surface is slowed down.

Moreover, with the increase of the surface roughness, the variations of the displacement thickness (δ_d/δ) and the momentum thickness (δ_m/δ_m) are presented in Fig. 10. For cases with small surface roughness (R_q = 0.0, 2.5 μm), the enhancement of the surface microstructures on the momentum mixing effect is limited, leading to a rather gentle growth of the displacement thickness and the momentum thickness. For cases with moderate surface roughness (R_q = 2.5, 5.0, 7.5 μm), the transportation of momentum is greatly promoted by the complicated vortex structures. Hence, the displacement thickness and the momentum thickness increase considerably. For cases with large surface roughness (R_q = 7.5, 10.0, 12.5 μm), the enhancement of the surface microstructures on the momentum mixing effect seems to be saturated, and the growth of the displacement thickness and the momentum thickness is flattened again.

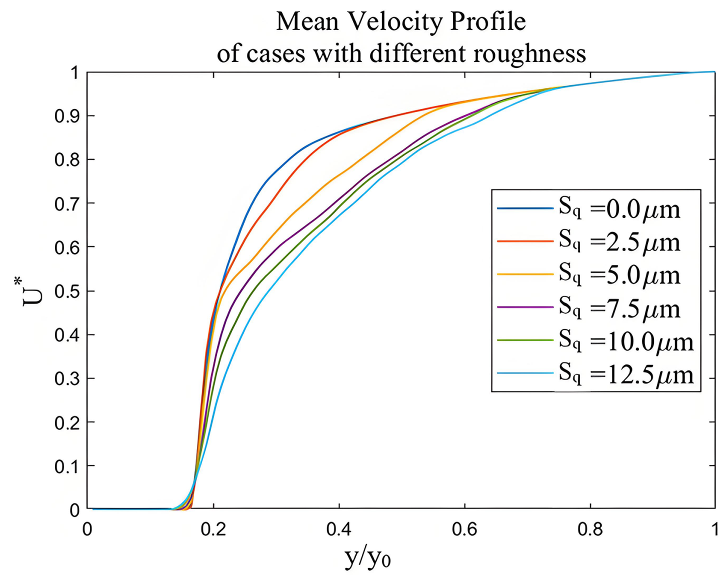

Figure 8: Mean velocity profile for cases with different surface roughness.

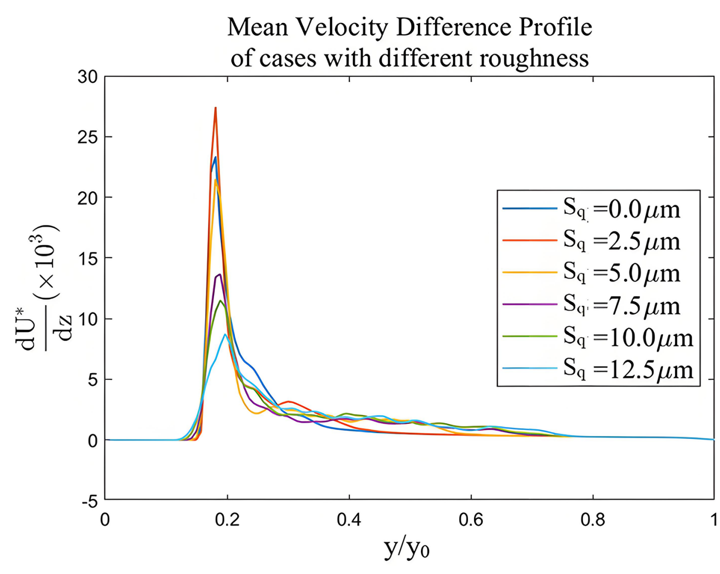

Figure 9: Mean velocity difference profile for cases with different surface roughness.

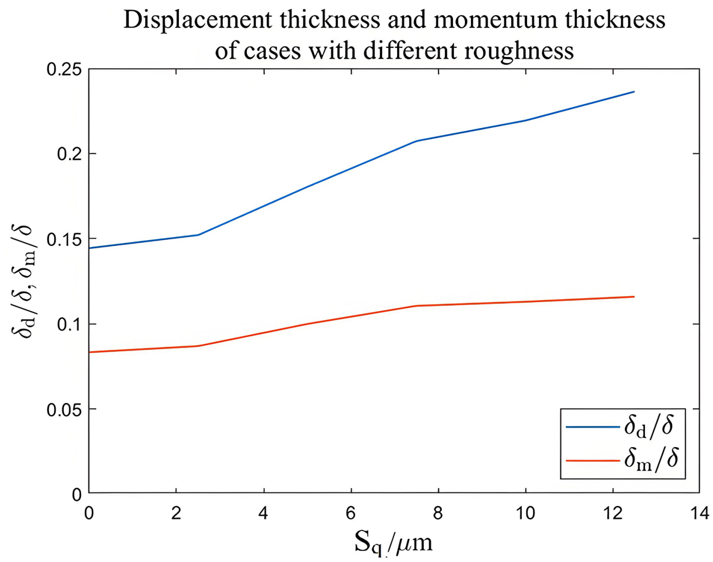

Figure 10: Displacement thickness and momentum thickness of cases with different surface roughness (S_q = 0.0, 2.5, 5.0, 7.5, 10.0, 12.5 μm).

3.2.4 Shear Stress Distribution on Thermal Barrier Coating Surface

The flow behaviors of the cooling film are changed greatly due to the roughness microstructures of the TBC surface, and in turn, the change of flow behaviors can also affect the mechanical load of the TBC. The shear stress distribution on the TBC surface is shown in Fig. 11. As the roughness increases, the shear stress distributed on the peaks of the surface microstructures increases greatly, while the shear stress distributed in the valleys of the surface microstructures decreases considerably. A drastic increase of the non-uniformity of the shear stress distribution is observed, which will accelerate the aging of TBC, and will easily cause cracks and even flaking of TBC, thus shortening the service life of TBC. These phenomena can be mainly attributed to the surface roughness microstructures, which lead to the fluctuation of the surface height distribution and local velocity difference at different positions of the TBC surface.

3.2.5 Mean Fanning Friction Factor on Thermal Barrier Coating Surface

The mean Fanning friction factor of each case is obtained by averaging the shear stress distribution on the TBC surface, as shown in Fig. 12. With the increase of the surface roughness, the mean Fanning friction factor increases at first and then fluctuates around 2.583 $\left(\overline{C_f}\right)_0$. Taking into account that the mean surface roughness has a strong relation with the velocity distribution near the wall, a further postprocess is done by calculating the ratio of the mean Fanning friction factor to the mean velocity difference at y = 100 μm. The relation between the mean square root roughness and the ratio of the mean Fanning friction factor to the mean velocity difference near the TBC surface is nearly linear, as shown in Fig. 13.

According to Figs. 12 and 13, it is assumed that the influence of the surface roughness on the mean Fanning friction factor of the TBC surface can be separated as 2 parts. The first part is the change of the mean velocity profile, which can be attributed to the enhancement of the momentum transportation induced by the surface roughness. The change of the mean velocity profile determines the magnitude of the mean velocity difference near the wall. The second part is the variation of the statistical properties of the shear stress distribution, which is ascribed to the deviation of local velocity difference from the mean velocity difference due to the surface height distribution of the exact surface morphology. Therefore, the overall influence of the surface roughness on the mean Fanning friction factor in similar cases concerning the prediction of the drag of turbulent flow over a rough surface, can be estimated by the product of the mean velocity profile acquired by experiments of simulations and a linear estimation representing the second part.

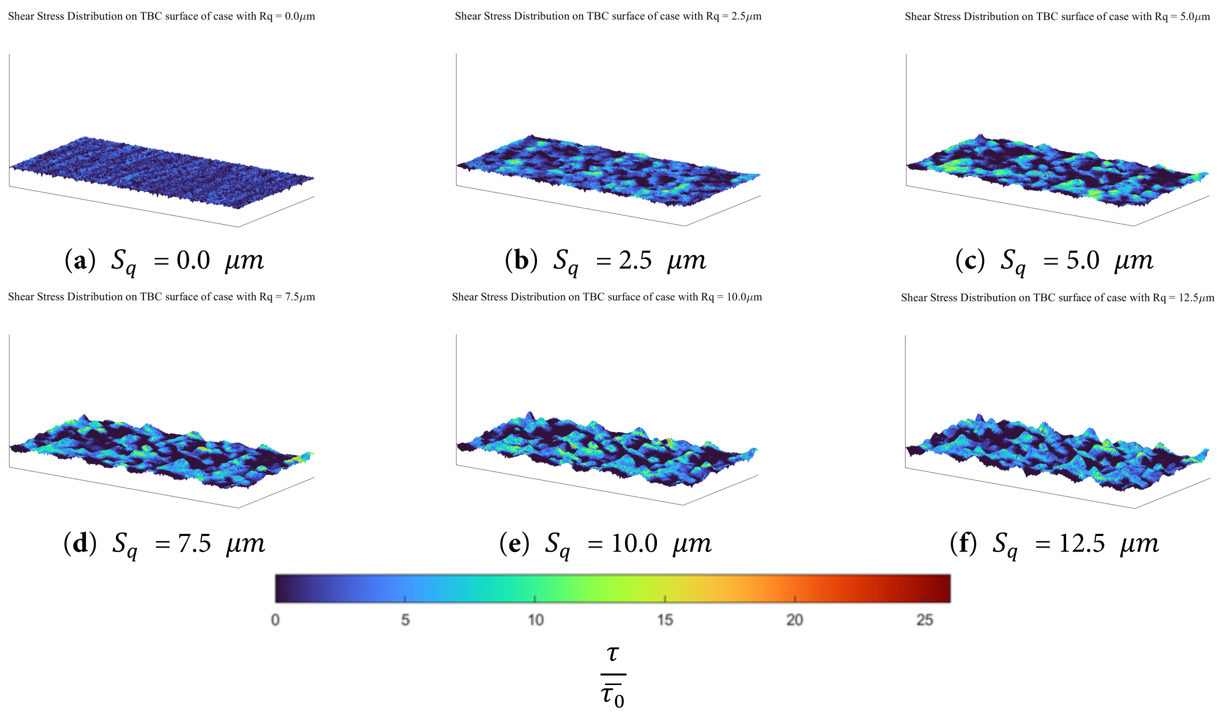

Figure 11: Shear stress distribution for cases with different surface roughness (S_q = 0.0, 2.5, 5.0, 7.5, 10.0, 12.5 μm), non-dimensionalized with mean shear stress of case with S_q = 0.0 μm.

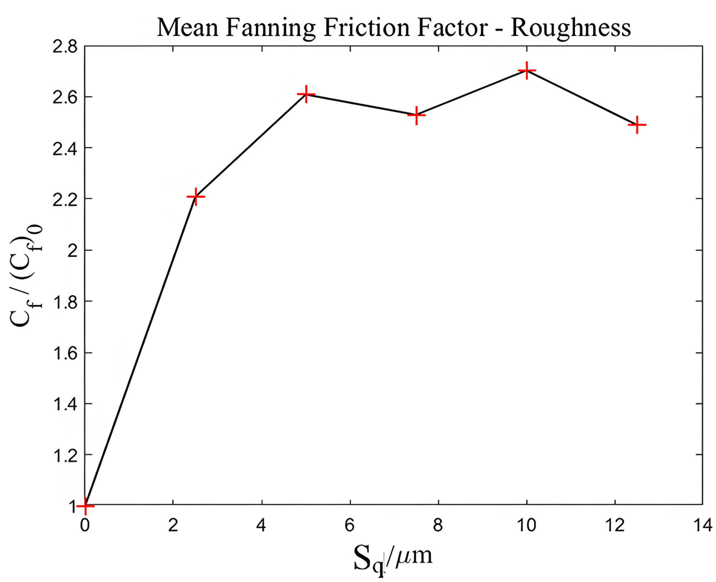

Figure 12: The relation of mean Fanning friction factor to surface roughness.

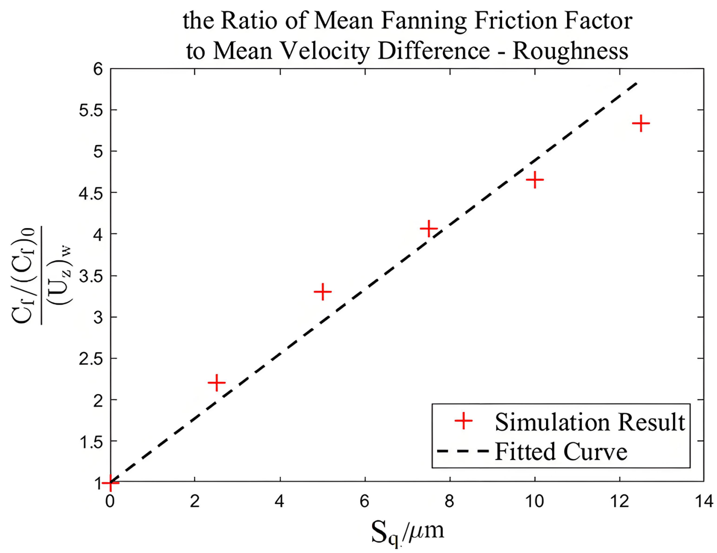

Figure 13: The relation between the ratio of mean Fanning friction factor to mean velocity difference (near the wall) and surface roughness.

3.3 Heat Transfer Performance of Cooling Film and Thermal Barrier Coating

The surface roughness not only influences the flow behaviors of the cooling film by increasing the fluctuation, changing the vortex structures, and enhancing the mixing effect, but makes notable impacts on the performance of the inter-coupled heat transfer process between the cooling film and TBC as well. In the following sections, the heat transfer performances concerning the insulation effectiveness and the deterioration of TBC, such as the temperature distribution on the TBC surface and the mean heat transfer coefficient, were studied.

3.3.1 Temperature Distribution of the Thermal Barrier Coating Surface

The variation of the flow behaviors always affects the heat transport properties of the flow, and thus the influence of the surface roughness on the temperature distribution of the TBC surface, whose non-uniformity may lead to the rise of the thermal stress, is worth to be reckoned with. The temperature distribution of the TBC surface is shown in Fig. 14. With the increase of surface roughness, it is noted that the statistical properties of the surface temperature distribution vary a lot. The average of the non-dimensional temperature on the TBC surface rises about 130%, and the maximum of the non-dimensional temperature on the TBC surface rises about 1162%, when the surface roughness increases from R_q = 0 μm to R_q = 12.5 μm. Additionally, a near-linear relation between the variance of the surface temperature distribution and the variance of the surface roughness distribution is observed, as shown in Fig. 15.

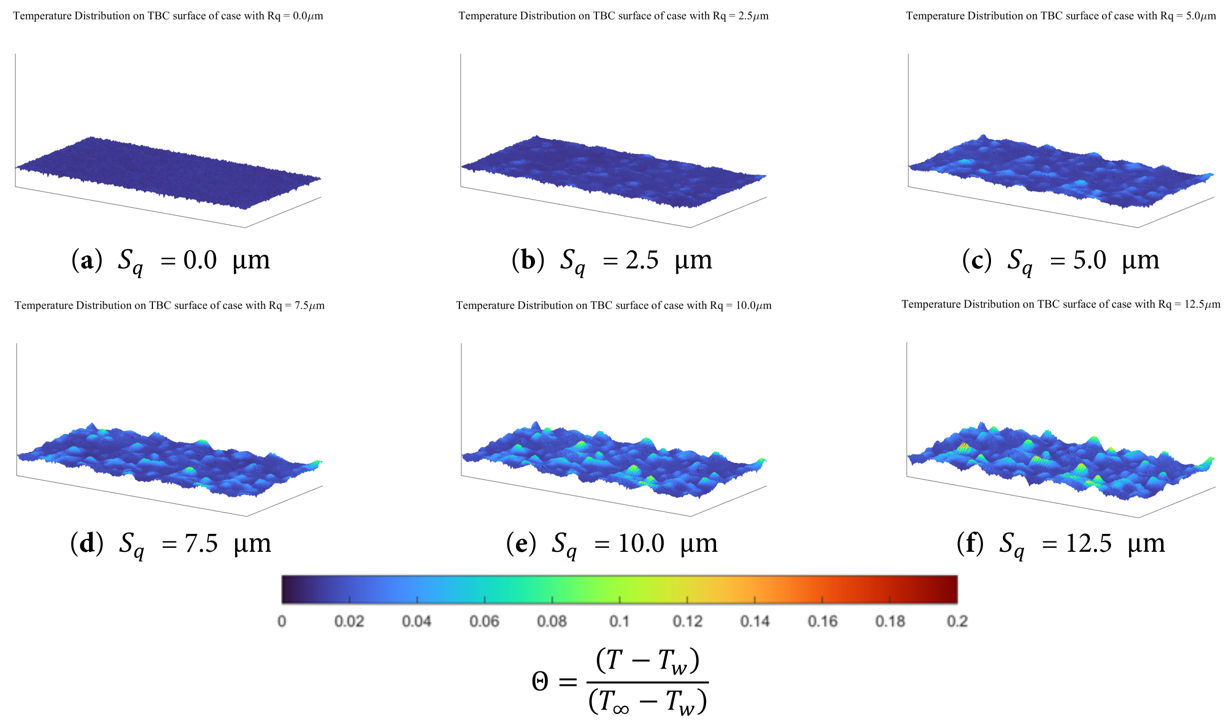

Figure 14: Non-dimensional temperature distribution on the TBC surface for cases with different surface roughness.

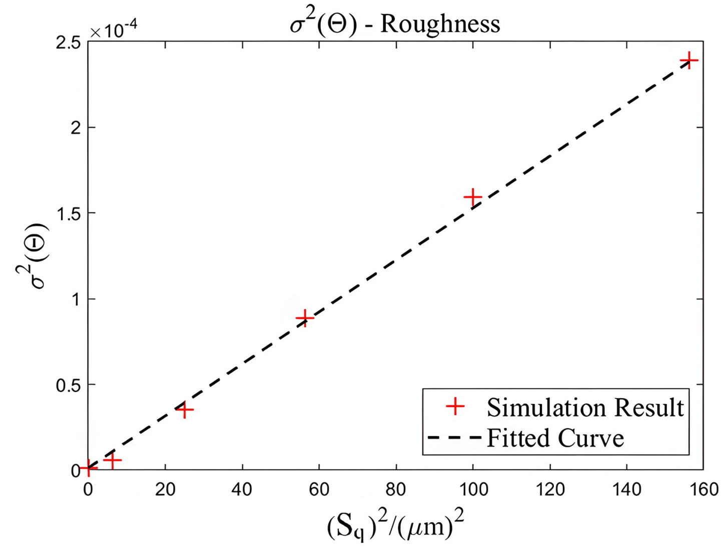

Figure 15: The relation between variance of non-dimensional temperature distribution on the TBC surface and variance of surface roughness.

3.3.2 Field Synergy Distribution in the Convectional Heat Transfer

The Field Synergy principle developed by Guo et al. [45] provides an insight into the mechanism of the convectional heat transfer in boundary layer flow. By studying the analogy between the heat convection and the heat conduction, it is found that the convectional heat transfer equation can be written in the form of a conduction heat transfer equation with the convection term regarded as a special source term.

$$\begin{cases} \rho C_p \left(\vec{u} \cdot \vec{\nabla}\right) T = \dfrac{\partial}{\partial z}\left(\lambda \dfrac{\partial T}{\partial z}\right) \\ -\dot{q} = \dfrac{\partial}{\partial z}\left(\lambda \dfrac{\partial T}{\partial z}\right) \end{cases} \tag{23}$$

And by applying integral on the convectional heat transfer equation over the thermal boundary layer, it is noted that the effect of the convection on the heat transfer can be separated from the equation and evaluated by the integral of the source term. In this work, the temperature gradient at the upper boundary should be taken into consideration as well.

$$\int_0^{\delta_t} \rho C_p \left(\vec{u} \cdot \vec{\nabla}\right) T dz = \lambda \left(\frac{\partial T}{\partial z}\right)_\infty - \lambda \left(\frac{\partial T}{\partial z}\right)_w \tag{24}$$

For turbulent flow [46], the time-averaging energy equation can be written as:

$$\rho C_p \left(\vec{u} \cdot \vec{\nabla}\right) T = \frac{\partial}{\partial z}\left(\left(\lambda + \rho C_p \alpha_t\right) \frac{\partial T}{\partial z}\right) \tag{25}$$

In the equation above, the α_t stands for the turbulent thermal diffusivity. By applying integration over the entire domain and Gauss theorem, a similar conclusion can be derived as well.

$$\begin{aligned} \iiint_\Omega \rho C_p \left(\vec{u} \cdot \vec{\nabla}\right) T \, d\Omega &= \iint_\infty \left(\lambda + \rho C_p \alpha_t\right) \frac{\partial T}{\partial z} dS - \iint_{wall} \left(\lambda + \rho C_p \alpha_t\right) \frac{\partial T}{\partial z} dS \\ &= \iint_\infty \left(\lambda + \rho C_p \alpha_t\right) \frac{\partial T}{\partial z} dS - \iint_{wall} \lambda \frac{\partial T}{\partial z} dS \end{aligned} \tag{26}$$

The equation can be further rewritten in a non-dimensional form. The cosine of the included angle of the velocity vector and the temperature gradient vector, which represents the synergy of the velocity field and the temperature gradient field, is closely related with the Nusselt number.

$$\begin{aligned} \iiint_\Omega \left(\frac{\vec{u}}{U_\infty} \cdot \vec{\nabla}\right) \frac{T}{\left(\frac{T_\infty - T_w}{\delta_t}\right)} \frac{1}{\delta_t} d\Omega &= \iiint_\Omega \cos\beta \frac{1}{\delta_t} d\Omega \\ &= \iint_\infty \frac{Nu_x}{Re_x Pr_{tot}} dS + \iint_{wall} \frac{Nu_x}{Re_x Pr} dS \end{aligned} \tag{27}$$

In the equation, the Pr_{tot} is the Prandtl number considering both the thermal diffusivity and the turbulent thermal diffusivity.

$$Pr_{tot} = \frac{\nu}{\alpha + \alpha_t} = \frac{\mu C_p}{\lambda + \rho C_p \alpha_t} \tag{28}$$

In order to throw lights on the mechanism of the influence of surface roughness on the convectional heat transfer, the included angle ($\cos\beta$) distribution of each case is calculated and presented in Fig. 16. According to Fig. 16, for the case with no surface roughness microstructures (R_q = 0.0 μm), the included angle between the velocity vectors and the temperature gradient vectors are around 90° in most of the regions away from the TBC surface, and some scattered fluctuations of the field synergy occur in the immediate adjacency of the TBC surface, which can be attributed to the interactions between the porous media and the flow.

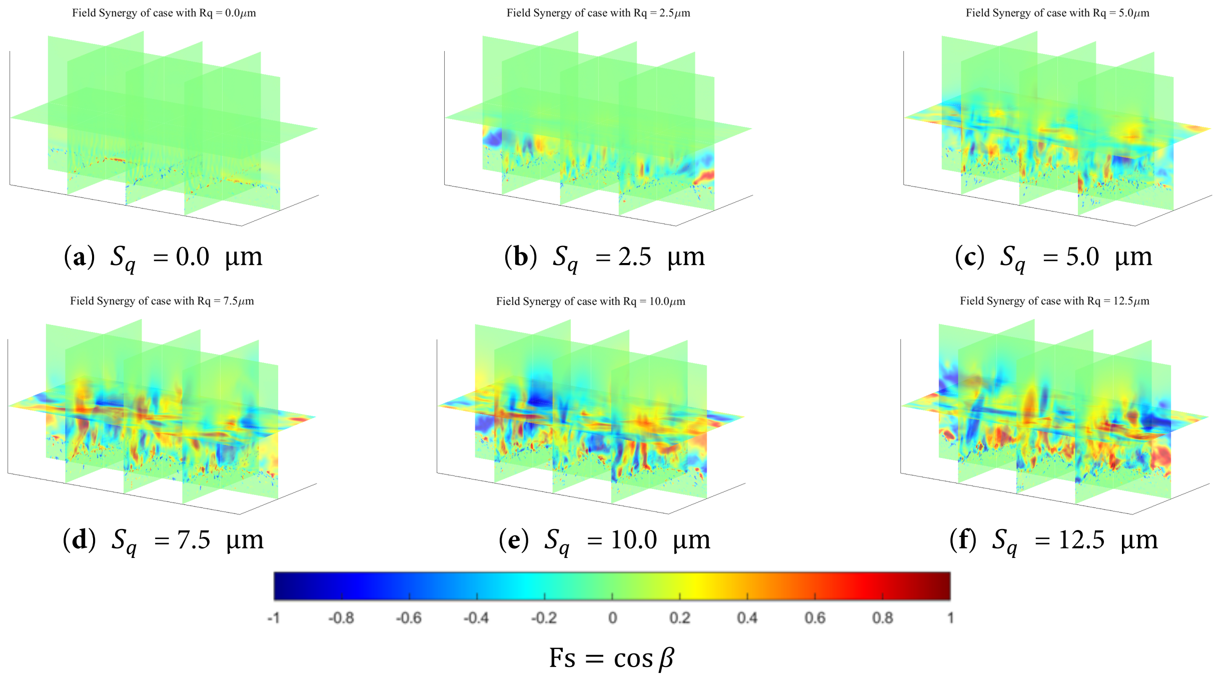

Figure 16: Distribution of included angle between the velocity vector and the temperature gradient vector for cases with different surface roughness.

When the surface roughness increases (R_q = 2.5, 5.0, 7.5 μm), accompanied by the change of the flow behaviors, the field synergy distribution is also influenced by the surface roughness. With the increase of the surface roughness, both the region positively and negatively influenced by convection in terms of heat transfer are expanding. For cases with surface roughness large enough (R_q = 10.0, 12.5 μm), the contribution of the surface roughness to the field synergy seems to be "saturated". With the same increment of the surface roughness, smaller variation of the field synergy distribution of case with rougher surface is observed, which is in good accordance with the conclusion of the vortex structures discussed in Section 3.2.2.

3.3.3 Mean Heat Transfer Coefficient

In the system composed of a 540 μm thick cooling film and a 100 μm thick TBC, the thermal resistance is dominated by the convectional heat transfer process which contributes to the majority part of the temperature drop, according to the temperature distribution on TBC surface. The relation of mean heat transfer coefficient to surface roughness is presented in Fig. 17. The result shows good accordance with the conclusion which has been drawn in Sections 3.2.2 and 3.2.3, that the enhancement of the surface roughness to the field synergy and the convectional heat transfer seems to be saturated gradually. The higher coating surface roughness also improves the heat transfer strength of the coating surface due to the increased heat transfer area and the disturbance to the flow. As the surface roughness of TBC increased, the convective heat transfer coefficient also gradually increased, with a maximum increase of 19.21%.

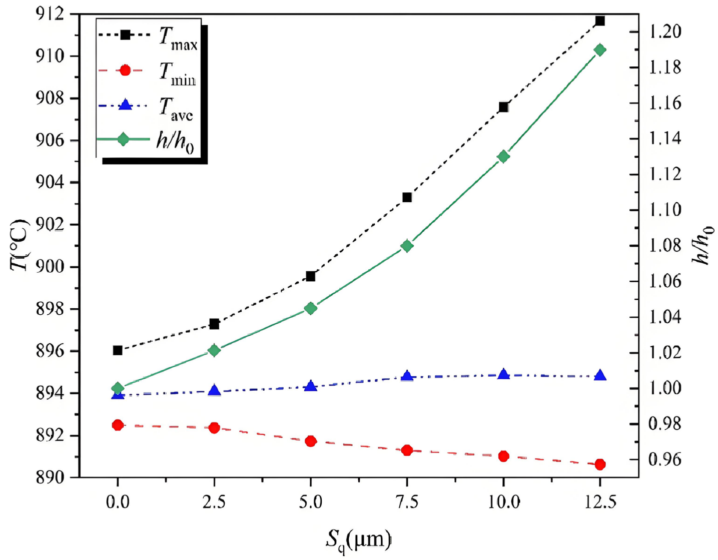

Figure 17: Characteristic temperature and convective heat transfer coefficient of TBC surface.

4 Conclusions

In this work, the effects of TBC surface roughness ($S_q = 0.0, 2.5, 5.0, 7.5, 10.0, 12.5$ μm) on the flow behaviors of cooling films and the conjugate heat transfer properties between the cooling film and TBC were investigated using DDF-LBM with LES. The key contributions of this study are summarized as follows:

1. The increase in TBC surface roughness substantially enhances the flow mixing effect, as evidenced by more widespread vortex distributions (identified by Ω criterion), alterations to the mean velocity profile, and increases in both the displacement and momentum thicknesses of the boundary layer.
2. The shear stress and temperature distribution on the TBC surface with greater roughness exhibit pronounced non-uniformity, which may induce cracking due to uneven mechanical loads and thermal stresses, thereby accelerating TBC deterioration.
3. As surface roughness increases, the mean Fanning friction factor initially rises and subsequently fluctuates around 2.583 $\left(\overline{C_f}\right)_0$. The influence of surface roughness on the mean Fanning friction factor can be divided into two parts: the first is the variation in mean velocity difference, induced by enhanced momentum transport; the second is the deviation of local velocity differences from the mean velocity difference, attributed to the height distribution of the uneven surface morphology. For similar cases involving drag prediction of turbulent flow over rough surfaces, the first part can be obtained through simulation or experiment, while the second part can be estimated using a near-linear relationship.
4. The statistical characteristics of the surface temperature distribution vary significantly with increasing surface roughness. The mean nondimensional temperature of TBC surface increases by approximately 130%, while the maximum nondimensional temperature rises by about 1162%.
5. Surface roughness augmentation also enhances heat transfer, with the convective heat transfer coefficient increasing progressively by a maximum of 19.21%. However, the rate of heat transfer enhancement diminishes gradually, a phenomenon attributable to the progressively saturated field synergy distribution.

Looking ahead, in order to improve computational accuracy and explore broader applications of micro-scale research findings in the design of turbine blades, it is recommended that research continue to be conducted in the following areas:

- To improve the accuracy of near-wall calculations, it is recommended that further research and development be conducted on dynamic LES models. The Smagorinsky number is calculated dynamically based on the turbulence characteristics of different flow regions.
- Further synthesize the link between micro-scale and macro-scale research findings to offer constructive recommendations for composite cooling technologies for turbine blades.
- Based on SEM images showing the evolution of the surface structure of thermal barrier coatings on gas turbine blades over varying service periods, this study investigates the degradation patterns of the cooling efficiency of turbine blades under different service conditions.

Acknowledgement: Not applicable.

Funding Statement: This research was funded by National Major Science and Technology Projects (2017-I-0007-0008) of China.

Author Contributions: The authors confirm contribution to the paper as follows: Conceptualization, Yuzhang Wang; methodology, Zhuning Liu and Zhuo Li; software, Zhuning Liu, Haozhe Sun and Chaoran Yang; validation, Yuzhang Wang, Zhuning Liu and Kanru Cheng; formal analysis, Zhuning Liu; investigation, Yuzhang Wang; resources, Yuzhang Wang; data curation, Zhuning Liu; writing—original draft preparation, Zhuning Liu; writing—review and editing, Yuzhang Wang; supervision, Yuzhang Wang; project administration, Yuzhang Wang; funding acquisition, Yuzhang Wang. All authors reviewed and approved the final version of the manuscript.

Availability of Data and Materials: Not applicable.

Ethics Approval: Not applicable.

Conflicts of Interest: The authors declare no conflicts of interest.

Nomenclature

A	Total area of the surface (m^2)
C	Smagorinsky constant
C_f	Fanning friction factor
$\left(\overline{C_f}\right)_0$	Mean Fanning friction factor of cases with R_q = 0 μm
c_p	Specific heat at constant pressure ($J \cdot m^{-2} \cdot K^{-1}$)
c_s	Lattice sound speed ($m \cdot s^{-1}$)
c_s^2	Square of the lattice sound velocity
$\vec{e_\alpha}$	Velocity set ($m \cdot s^{-1}$)
$\overline{f_i}$	Probability density function
$f_\alpha(\vec{r}, t)$	Particle distribution function of density
$f_\alpha^{eq}(\vec{r}, t)$	Equilibrium distribution function of density
Fs, $\cos\beta$	Field synergy, the cosine of the included angle
$g_\alpha(\vec{r}, t)$	Particle distribution function of temperature
$g_\alpha^{eq}(\vec{r}, t)$	Equilibrium distribution function of temperature
$G(x, x')$	Generating Functions for 3D Grids
$h(x, y)$	Filter coefficient
$H\left(\omega_x, \omega_y\right)$	Transfer function
k, l	Discrete offset coordinates
l	Lattice length
l_x, l_y	autocorrelation length
m, n	Number of discrete sampling points
q	Heat flux density ($W \cdot m^{-2}$)

$\vec{r}$	Spatial position vectors
S	Local strain tensor
S_a	Arithmetic mean roughness (μm)
S_q	Mean square root roughness (μm)
S_{sk}	Skewness
S_{ku}	Kurtosis
$S(x, y)$	Original signal at the position (x, y)
$S(\omega_x, \omega_y)$	Power spectral density of the input signal
$S_\eta(\omega_x, \omega_y)$	Power spectral density of the original surface roughness of the measured surface
t	Time (s)
T_∞	Temperature at the top of the cooling film (K)
T_w	Temperature at the bottom of the TBC (K)
$\vec{u}$	Velocity ($m \cdot s^{-1}$)
U^*	Mean velocity (along the x-y plane) ($m \cdot s^{-1}$)
U_∞	Velocity at the top of the cooling film ($m \cdot s^{-1}$)
$\vec{v}$	Discrete velocity vector ($m \cdot s^{-1}$)
V_{A^+}	Van Driest damping function
w_i	Weight coefficient
x, y	Cartesian coordinates in space (m)
y^+	Dimensionless wall normal distance
$z(i, j)$	Roughness height distribution (μm)
α	Thermal diffusivity ($m^2 \cdot s^{-1}$)
α_t	Turbulent diffusion coefficient ($m^2 \cdot s^{-1}$)
ν_e, ν, ν_t	Eddy viscosity ($m^2 \cdot s^{-1}$), molecular viscosity ($m^2 \cdot s^{-1}$), total viscosity
$\eta(x, y)$	two-dimensional surface elevation profile
ω_x, ω_y	Spatial angular frequency
$\overline{\lambda_{exp}}, \overline{\lambda_{cal}}$	Effective heat conductivity (experiment and simulation result) ($W \cdot m^{-1} \cdot K^{-1}$)
λ_1, λ_2	Thermal conductivity of air and YSZ ($W \cdot m^{-1} \cdot K^{-1}$)
τ, τ_f, t_g	Relaxation time
ρ	Density ($kg \cdot m^{-3}$)
Θ	Non-dimensional temperature
Ω	Ω criterion
$\frac{\delta_d}{\delta}, \frac{\delta_m}{\delta}$	Displacement and momentum thickness of the boundary layer

References

1. Padture NP. Advanced structural ceramics in aerospace propulsion. Nat Mater. 2016;15(8):804–9. doi:10.1038/nmat4687.
2. Wang Y, Liu H, Ling X, Weng Y. Effects of pore microstructure on the effective thermal conductivity of thermal barrier coatings. Appl Therm Eng. 2016;102(1):234–42. doi:10.1016/j.applthermaleng.2016.03.174.
3. Chen X, Wang Y, Long Y, Weng S. Effect of particle deposition on film cooling from fan-shaped holes. Int J Heat Mass Transf. 2021;181(5):122028. doi:10.1016/j.ijheatmasstransfer.2021.122028.
4. Wang Y, Li J, Liu H, Weng Y. Study on thermal resistance performance of 8YSZ thermal barrier coatings. Int J Therm Sci. 2017;122(1):12–25. doi:10.1016/j.ijthermalsci.2017.08.006.
5. Park K, Kim K, Kim D, Moon B, Park S, Seok CS. Failure mechanism of plasma-sprayed thermal barrier coatings under high-temperature isothermal aging conditions. Ceram Int. 2021;47(11):15883–900. doi:10.1016/j.ceramint.2021.02.163.

6. Song JB, Wang LS, Dong H, Yao JT. Long lifespan thermal barrier coatings overview: materials, manufacturing, failure mechanisms, and multiscale structural design. Ceram Int. 2023;49(1):1–23. doi:10.1016/j.ceramint.2022.10.222.
7. Unnikrishnan U, Yang V. A review of cooling technologies for high temperature rotating components in gas turbine. Propuls Power Res. 2022;11(3):293–310. doi:10.1016/j.jppr.2022.07.001.
8. Ellis CD, Xia H. Impact of inflow turbulence on large-eddy simulation of film cooling flows. Int J Heat Mass Transf. 2022;195(5):123172. doi:10.1016/j.ijheatmasstransfer.2022.123172.
9. Zhang G, Zhu R, Xie G, Li S, Sundén B. Optimization of cooling structures in gas turbines: a review. Chin J Aeronaut. 2022;35(6):18–46. doi:10.1016/j.cja.2021.08.029.
10. Chen X, Wang Y, Long Y, Weng S. Effect of partial blockage on flow and heat transfer of film cooling with cylindrical and fan-shaped holes. Int J Therm Sci. 2021;164:106866. doi:10.1016/j.ijthermalsci.2021.106866.
11. Bons JP, Taylor RP, McClain ST, Rivir RB. The many faces of turbine surface roughness. J Turbomach. 2001;123(4):739–48. doi:10.1115/1.1400115.
12. Chen X, Long Y, Wang Y, Weng S, Luan Y. Large eddy simulation of film cooling from cylindrical holes partially blocked by CaO-MgO-Al_2O_3-SiO_2. Int Commun Heat Mass Transf. 2021;129:105754. doi:10.1016/j.icheatmasstransfer.2021.105754.
13. Lashmi PG, Ananthapadmanabhan PV, Unnikrishnan G, Aruna ST. Present status and future prospects of plasma sprayed multilayered thermal barrier coating systems. J Eur Ceram Soc. 2020;40(8):2731–45. doi:10.1016/j.jeurceramsoc.2020.03.016.
14. Luo L, Chen Y, Zhou M, Shan X, Lu J, Zhao X. Progress update on extending the durability of air plasma sprayed thermal barrier coatings. Ceram Int. 2022;48(13):18021–34. doi:10.1016/j.ceramint.2022.04.044.
15. Li GR, Yang GJ, Li CX, Li CJ. Sintering characteristics of plasma-sprayed TBCs: experimental analysis and an overall modelling. Ceram Int. 2018;44(3):2982–90. doi:10.1016/j.ceramint.2017.11.052.
16. Stewart WR, Kistenmacher DA, Bogard DG. Effects of TBC thickness on an internally and film cooled model turbine vane. In: Proceedings of the ASME Turbo Expo 2014: Turbine Technical Conference and Exposition; 2014 Jun 16–20; Düsseldorf, Germany. doi:10.1115/gt2014-27117.
17. Long Y, Chen X, Wang Y, Weng Y. Conjugate flow and heat transfer analysis between segmented thermal barrier coatings and cooling film. Int J Therm Sci. 2021;167(3):107003. doi:10.1016/j.ijthermalsci.2021.107003.
18. Nguyen DH, Ahn HS. A comprehensive review on micro/nanoscale surface modification techniques for heat transfer enhancement in heat exchanger. Int J Heat Mass Transf. 2021;178(11):121601. doi:10.1016/j.ijheatmasstransfer.2021.121601.
19. Chung D, Hutchins N, Schultz MP, Flack KA. Predicting the drag of rough surfaces. Annu Rev Fluid Mech. 2021;53(1):439–71. doi:10.1146/annurev-fluid-062520-115127.
20. Everts M, Robbertse P, Spitholt B. The effects of surface roughness on fully developed laminar and transitional flow friction factors and heat transfer coefficients in horizontal circular tubes. Int J Heat Mass Transf. 2022;189(1):122724. doi:10.1016/j.ijheatmasstransfer.2022.122724.
21. Ma R, Alamé K, Mahesh K. Direct numerical simulation of turbulent channel flow over random rough surfaces. J Fluid Mech. 2021;908:A40. doi:10.1017/jfm.2020.874.
22. MacDonald M, Hutchins N, Chung D. Roughness effects in turbulent forced convection. J Fluid Mech. 2019;861:138–62. doi:10.1017/jfm.2018.900.
23. Zhang Y, Chai J. Effect of surface morphology on fluid flow in rough fractures: a review. J Nat Gas Sci Eng. 2020;79(6):103343. doi:10.1016/j.jngse.2020.103343.
24. Nardini M, Kozul M, Jelly TO, Sandberg RD. Direct numerical simulation of transitional and turbulent flows over multi-scale surface roughness: part I: methodology and challenges. J Turbomach. 2024;146(3):031008. doi:10.1115/1.4063753.
25. Kadivar M, Tormey D, McGranaghan G. A review on turbulent flow over rough surfaces: fundamentals and theories. Int J Thermofluids. 2021;10(151):100077. doi:10.1016/j.ijft.2021.100077.
26. Pawlus P, Reizer R, Wieczorowski M. A review of methods of random surface topography modeling. Tribol Int. 2020;152:106530. doi:10.1016/j.triboint.2020.106530.

27. Wang M, Wang J, Pan N, Chen S. Mesoscopic predictions of the effective thermal conductivity for microscale random porous media. Phys Rev E. 2007;75(3):036702. doi:10.1103/physreve.75.036702.
28. Long Y, Wang Y, Chen X, Sang R. 3D numerical reconstruction and microstructure regulation of thermal barrier coatings for high temperature components of gas turbine. Ceram Int. 2021;47(14):20126–40. doi:10.1016/j.ceramint.2021.04.019.
29. He YL, Liu Q, Li Q, Tao WQ. Lattice Boltzmann methods for single-phase and solid-liquid phase-change heat transfer in porous media: a review. Int J Heat Mass Transf. 2019;129(4):160–97. doi:10.1016/j.ijheatmasstransfer.2018.08.135.
30. McNamara GR, Zanetti G. Use of the Boltzmann equation to simulate lattice gas automata. Phys Rev Lett. 1988;61(20):2332–5. doi:10.1103/PhysRevLett.61.2332.
31. He X, Luo LS. Theory of the lattice Boltzmann method: from the Boltzmann equation to the lattice Boltzmann equation. Phys Rev E. 1997;56(6):6811–7. doi:10.1103/physreve.56.6811.
32. He X, Chen S, Doolen GD. A novel thermal model for the lattice Boltzmann method in incompressible limit. J Comput Phys. 1998;146(1):282–300. doi:10.1006/jcph.1998.6057.
33. Husson J, Terracol M, Deck S, Le Garrec T. A comprehensive framework for robust hybrid RANS/LES simulations of wall-bounded flows in LBM. J Comput Phys. 2024;502(4):112814. doi:10.1016/j.jcp.2024.112814.
34. Kuwata Y, Suga K. Lattice Boltzmann direct numerical simulation of interface turbulence over porous and rough walls. Int J Heat Fluid Flow. 2016;61(1):145–57. doi:10.1016/j.ijheatfluidflow.2016.03.006.
35. Kuwata Y, Suga K. Wall-modeled large eddy simulation of turbulent heat transfer by the lattice Boltzmann method. J Comput Phys. 2021;433(1):110186. doi:10.1016/j.jcp.2021.110186.
36. Fischer L, Pfitzner M. Impact of external turbulence on film cooling designs using large eddy simulations. Int J Heat Mass Transf. 2023;217(4):124623. doi:10.1016/j.ijheatmasstransfer.2023.124623.
37. Zamiri A, You SJ, Chung JT. Surface roughness effects on film-cooling effectiveness in a fan-shaped cooling hole. Aerosp Sci Technol. 2021;119:107082. doi:10.1016/j.ast.2021.107082.
38. Bhatnagar PL, Gross EP, Krook M. A model for collision processes in gases. I. Small amplitude processes in charged and neutral one-component systems. Phys Rev. 1954;94(3):511–25. doi:10.1103/physrev.94.511.
39. Guo S, Feng Y, Jacob J, Renard F, Sagaut P. An efficient lattice Boltzmann method for compressible aerodynamics on D3Q19 lattice. J Comput Phys. 2020;418(2):109570. doi:10.1016/j.jcp.2020.109570.
40. Malaspinas O, Sagaut P. Wall model for large-eddy simulation based on the lattice Boltzmann method. J Comput Phys. 2014;275(1):25–40. doi:10.1016/j.jcp.2014.06.020.
41. Lee M, Moser RD. Direct numerical simulation of turbulent channel flow up to Re-tau approximate to 5200. J Fluid Mech. 2015;774:395–415. doi:10.1017/jfm.2015.268.
42. Yao J, Rezaeiravesh S, Schlatter P, Hussain F. Direct numerical simulations of turbulent pipe flow up to. J Fluid Mech. 2023;956:A18. doi:10.1017/jfm.2022.1013.
43. Zhang YN, Qiu X, Chen FP, Liu KH, Dong XR, Liu C. A selected review of vortex identification methods with applications. J Hydrodyn. 2018;30(5):767–79. doi:10.1007/s42241-018-0112-8.
44. Liu C, Wang Y, Yang Y, Duan Z. New omega vortex identification method. Sci China Phys Mech Astron. 2016;59(8):684711. doi:10.1007/s11433-016-0022-6.
45. Guo ZY, Li DY, Wang BX. A novel concept for convective heat transfer enhancement. Int J Heat Mass Transf. 1998;41(14):2221–5. doi:10.1016/S0017-9310(97)00272-X.
46. Guo ZY, Tao WQ, Shah RK. The field synergy (coordination) principle and its applications in enhancing single phase convective heat transfer. Int J Heat Mass Transf. 2005;48(9):1797–807. doi:10.1016/j.ijheatmasstransfer.2004.11.007.